

Adaptive Plane Reformatting for 4D Flow MRI using Deep Reinforcement Learning

Javier Bisbal, Julio Sotelo, Maria I Valdés, Pablo Irarrazaval, Marcelo E Andia, Julio García, José Rodríguez-Palomarez, Francesca Raimondi, Cristián Tejos, and Sergio Uribe *

Deep reinforcement learning (DRL) algorithms have shown robust results in plane reformatting tasks. In these methods, an agent sequentially adjusts the position and orientation of an initial plane towards an objective location. This process allows accurate plane reformatting, without the need for detailed landmarks, which makes it suitable for images with limited contrast and resolution, such as 4D flow MRI. However, current DRL methods require the test dataset to be in the same position and orientation as the training dataset. In this paper, we present a novel technique that utilizes a flexible coordinate system based on the current state, enabling navigation in volumes at any position or orientation. We adopted the Asynchronous Advantage Actor Critic (A3C) algorithm for reinforcement learning, outperforming Deep Q Network

(DQN). Experimental results in 4D flow MRI demonstrate improved accuracy in plane reformatting angular and distance errors ($6.32^\circ \pm 4.15^\circ$ and 3.40 ± 2.75 mm), as well as statistically equivalent flow measurements determined by a plane reformatting process done by an expert ($p=0.21$). The method's flexibility and adaptability make it a promising candidate for other medical imaging applications beyond 4D flow MRI.

1 Introduction

Four-dimensional Phase Contrast Magnetic Resonance Imaging (PC-MRI), also known as 4D flow MRI, provides a time-resolved velocity field in a volumetric region of interest. 4D flow MRI quantifies advanced hemodynamics for cardiovascular disease assessment [1, 2, 3]. Although, 4D flow MRI facilitated the acquisition of whole heart and great vessels [4], its analysis is complex and time-consuming, and laborious planning is required for assessing different flow quantities retrospectively.

Positioning of planes within the volumetric region allows for specific hemodynamic analyses of different vessels within the heart, however the orientation of those planes in double oblique manner is challenging. Plane reformatting is typically carried out manually [5], which makes it user-dependent and time-consuming, especially when several vessels are analyzed as in congenital heart diseases such as Tetralogy of Fallot, aortic coarctation, or bicuspid aortic valve [6, 7].

Landmark localization has been a common approach for plane reformatting in MRI [8]. However, the relatively low spatial resolution of 4D flow MRI does not allow precise identification of landmarks necessary for accurate plane reformatting. Instead, techniques involving the navigation within 3D Phase Contrast Magnetic Resonance Angiography (PC-MRA) and flow pathlines or streamlines have been adopted for manual plane reformatting [5].

Automated plane reformatting have been introduced using atlas

*J. Bisbal, P. Irarrazaval, C. Tejos, M. Andia, M. Valdés are with the Biomedical Imaging Center, Pontificia Universidad Católica de Chile (PUC), Region Metropolitana, Santiago, CL. (e-mail: jebisbal, pim, ctejos, mandia@uc.cl, mivaldesvar@gmail.com). J. Bisbal, P. Irarrazaval and C. Tejos are with the Department of Electrical Engineering, School of Engineering, PUC, Region Metropolitana, Santiago, CL. J. Sotelo is with the Departamento de Informática, Universidad Técnica Federico Santa María, Santiago, CL. (e-mail: julio.sotelo@usm.cl). P. Irarrazaval is with Institute for Biological and Medical Engineering, School of Engineering, Medicine and Biological sciences, PUC, Region Metropolitana, Santiago, CL. M. Andia is with Department of Radiology, School of Medicine, PUC, Region Metropolitana, Santiago, CL. S.Uribe is with the department of Medical Imaging and Radiation Sciences, School of Primary and Allied Health Care. Faculty of Medicine, Nursing and Health Sciences. Monash University, Melbourne, AUS. (e-mail: sergio.uribe@monash.edu). J. Bisbal, P. Irarrazaval, C. Tejos, and M. Andia are with Millennium Institute for Intelligent Healthcare Engineering, iHEALTH, Region Metropolitana, Santiago, CL. J. García is with Stephenson Cardiac Imaging Centre, Departments of Radiology and Cardiac Sciences, University of Calgary, Calgary, AB, CAN. (e-mail: julio.garciaflores@ucalgary.ca). J. Rodríguez-Palomares is with Department of Cardiology, Vall d'Hebron Hospital Universitari, Vall d'Hebron Barcelona Hospital Campus, Barcelona, ESP; Cardiovascular Diseases, Vall d'Hebron Institut de Recerca (VHIR), Vall d'Hebron Barcelona Hospital Campus, Barcelona, ESP; Department of Medicine, Universitat Autònoma de Barcelona, Bellaterra, ESP; CIBER de Enfermedades Cardiovasculares, Instituto de Salud Carlos III, Madrid, ESP (e-mail: jfrodriiguezpalomares@gmail.com). F. Raimondi is with Department of Cardiology and Cardiovascular Surgery, Papa Giovanni XXIII Hospital, Bergamo, IT, and also with Hopital Necker Enfants Malades, Paris, FR. (e-mail: francesca.raimondi@gmail.com).

registration [9]. This method involves a deformable registration of imaging planes of an atlas with an input image, yielding promising outcomes. However, since it is computationally demanding and depends on image-atlas similarity, this approach has not been extensively used in clinical applications. More recently, a deep learning approach utilizing a 3D convolutional neural network (CNN) has demonstrated the potential to identify vessel patches and predict plane orientation [10]. However, its reliance on small vessel patches may overlook crucial information from surrounding structures.

Deep reinforcement learning (DRL) has also shown good results for automatic plane reformatting in MRI and ultrasound [11, 12, 13]. In this framework, a CNN-based agent sequentially predicts rotations and translations to update an initial plane towards an objective location. DRL obviates the need for landmarks; instead, it analyzes different structures in its navigation trajectory, making it particularly suitable for low-contrast images such as 4D flow MRI.

Nevertheless, existing DRL algorithms for plane reformatting perform rotations and translations with a fixed coordinate system defined by the MRI acquisition. This means that if test volumes differ in orientation or position from training data, the algorithm may fail to converge, needing pre-reformatting registration of all volumes to a consistent orientation and position. This requirement significantly restricts the use of databases from different institutions or vendors.

In this work, we present a novel DRL algorithm for adaptive plane reformatting in 4D flow MRI, at any orientation or position. Our approach employs an arbitrary coordinate system during plane transitions, thereby enabling flexibility and generalization across different orientations and positions.

2 Methods

2.1 Reinforcement learning framework

In reinforcement learning, an agent learns to make decisions by interacting with an environment, receiving rewards and refining its strategy to maximize the accumulated reward.

In a reinforcement learning task, an agent sequentially updates a state $s_t \in S$, by performing action $a_t \in A$ at step $t \in [t_0, t_{\max}]$. Here, S is the set of possible states within an environment E , while A represents the set of possible actions. For each transition $T(s_t, a_t, s_{t+1})$, i.e., for each action a_t with which the agent transits from state s_t to state s_{t+1} , we define reward $r_t \in \mathcal{R}$, with \mathcal{R} the set of possible rewards. Finally, a termination signal is triggered when the agent achieves a target state or exceeds t_{\max} steps. Upon receiving this signal, the environment is reset, and the agent starts a new sequence, often referred to as an episode.

For the task of plane reformatting in 4D flow MRI, we defined the following reinforcement learning framework:

2.1.1 Environment (E)

The environment where the agent navigates considers two sets of volumes:

3D Phase Contrast Magnetic Resonance Angiography (PC-MRA): this volume was computed as:

$$3D \text{ PC-MRA}(\vec{r}) = \sqrt{\frac{1}{N} \sum_{\tau=1}^N M_{\tau}^2(\vec{r}) \sum_{j=x,y,z} V_{(\tau,j)}^2(\vec{r})}, \quad (1)$$

with M_{τ} the magnitude of the 4D Flow MRI signal at timeframe τ ; $V_{(\tau,j)}$ the component j of the velocity at timeframe; \vec{r} the three-dimensional spatial location; and N the number of timeframes.

To reduce noise and enhance contrast between vascular and non-vascular regions, we adapted Eq. (1) to:

$$3D \text{ PC-MRA}(\vec{r}) = \sqrt{\frac{1}{N} \sum_{\tau=1}^N M_{\tau}^2(\vec{r}) \sum_{j=x,y,z} (V_{(\tau,j)}(\vec{r}) K_{\tau}(\vec{r}))^2}, \quad (2)$$

with,

$$K_t(\vec{r}) = 1 - \frac{\log(\text{std}(|\nabla \cdot \vec{V}_{\tau}(\vec{r})|))}{\max[\log(\text{std}(|\nabla \cdot \vec{V}_{\tau}(\vec{r})|))]},$$

where \vec{V}_{τ} represents the velocity vector at timeframe τ for the spatial location \vec{r} , $\nabla \cdot$ is the divergence operation on each spatial location \vec{r} , and $\text{std}()$ and $\max()$ represent the standard deviation along the time dimension and the maximum across all spatial dimensions, respectively. Essentially, we multiplied the velocity with values close to 1 where the standard deviation of the divergence was low (mass conservation), and values close to 0 where the standard deviation of the divergence was high (background noise).

Finally, to increase homogeneity between different 3D PC-MRA scans we performed Contrast Limited Adaptive Histogram Equalization (CLAHE) on the result of equation (2). Unlike standard histogram equalization, CLAHE avoids noise amplification. It works with two parameters, contextual region size, and clipping limit. For our 4D Flow MRI datasets we chose a contextual region of one-sixth of the original image size and a clipping limit of 1% [14].

Systolic velocities: To provide more information to the agent, we extracted velocities at peak systole using a threshold on the 3D PC-MRA image, ensuring peak timeframe evaluation only in vessel regions.

To decrease variability due to different resolutions, we scaled all data sets to an isotropic resolution of $2 \times 2 \times 2 \text{ mm}^3$ using trilinear interpolation. Following the reformatting process, this scaling was then reversed before flow computation.

2.1.2 States (S)

The plane being reformatted at step t is defined by a point (\vec{P}_t) = $P_t^x \hat{i} + P_t^y \hat{j} + P_t^z \hat{k}$ and an orthonormal basis $B = \{\vec{n}_t, \vec{w}_t^1, \vec{w}_t^2\}$, with $\vec{w}_t^1 = w_t^{1x} \hat{i} + w_t^{1y} \hat{j} + w_t^{1z} \hat{k}$, $\vec{w}_t^2 = w_t^{2x} \hat{i} + w_t^{2y} \hat{j} + w_t^{2z} \hat{k}$, and $\vec{n}_t = n_t^x \hat{i} + n_t^y \hat{j} + n_t^z \hat{k}$, where $\{\hat{i}, \hat{j}, \hat{k}\}$ are the coordinate unit vectors defined by the 4D flow MRI acquisition. Each state is then represented by an array of 3D sub-coordinates centered at \vec{P}_t with the first axis oriented along the (\vec{n}_t) vector direction, the second axis oriented along the \vec{w}_t^1 vector direction, and the third axis oriented along the \vec{w}_t^2 vector direction. The sub-coordinates have dimensions (D, H, W), where D, H and W correspond to depth, height, and width, respectively, with $2 \times 2 \times 2 \text{ mm}^3$ spacing.

Using these sub-coordinates, we sampled two sub-volumes via tri-linear interpolation: the first from the 3D PC-MRA volume, and the second containing the projections of the systolic velocities $V_t = \sqrt{(\vec{n}_t \cdot \vec{V}_{\text{sys}})^2}$ along (\vec{n}_t), where $\vec{V}_{\text{sys}} = V_{\text{sys}}^x \hat{i} + V_{\text{sys}}^y \hat{j} + V_{\text{sys}}^z \hat{k}$, and sys denotes velocities at the systolic timeframe.

Arbitrary coordinate system: To be able to work with volumes in different orientations or positions, our algorithm works

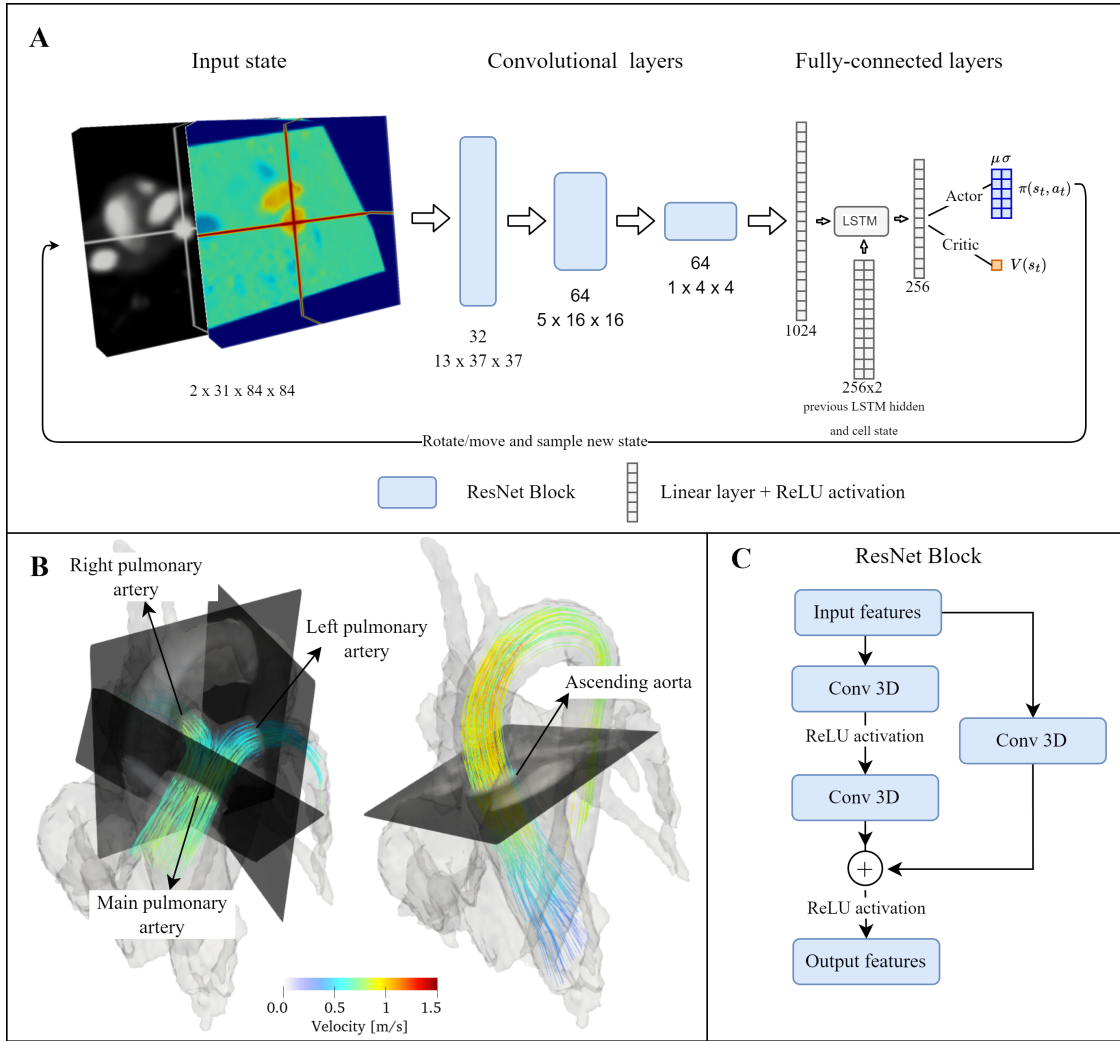


Figure 1: **A.** Reinforcement learning framework: An initial stack of volumes goes through three convolutional layers and 1 fully-connected layer. The output of this layer feeds an LSTM cell with the previous LSTM hidden and cell state. Next, the Actor layers compute μ_a and σ_a to estimate the policy $\pi(s, a)$ and the Critic layer estimates the value function $G(s)$. The model parameters are updated with equation (6) and the policy is sampled to transition to a new state. **B.** Example of manual reformatted planes used for training. **C.** Diagram of ResNet blocks in convolutional layers.

with an arbitrary coordinate system defined by B . To differentiate states with different bases, we defined imaginary axes that go through the center of each slice along the first dimension of each state, following the directions of \vec{w}_t^1 and \vec{w}_t^2 (see state of Fig. 1.A).

Initial state: For training, the first state (s_0) had a random location within 10% of the volume size around the center, and a random orientation. For reproducibility, validation and testing, we used a fixed location ($(\vec{P}_0) = \{0, 0, 0\}$) and orientation ($(\vec{n}_0 = \{1, 0, 0\})$).

2.1.3 Actions (A)

For state s_t with basis $\{\vec{n}, \vec{w}_1, \vec{w}_2\}_t$ the set of actions are defined as:

$$A_t = \{(r_{\vec{w}_t^1}, r_{\vec{w}_t^2}, m_{\vec{w}_t^1}, m_{\vec{w}_t^2}, m_{\vec{n}_t}) \mid s_t \in S\}, \quad (3)$$

$r_{\vec{w}_t^1}$ denotes a rotation of \vec{n}_t and \vec{w}_t^2 around the axis defined by \vec{w}_t^1 ; and $r_{\vec{w}_t^2}$ denotes a rotation of \vec{n}_t and \vec{w}_t^1 around the axis defined by \vec{w}_t^2 . Additionally, $m_{\vec{w}_t^1}, m_{\vec{w}_t^2}, m_{\vec{n}_t}$ denote translations of (\vec{P}_t) in the directions defined by \vec{w}_t^1, \vec{w}_t^2 , and \vec{n}_t , respectively.

Rotations are restricted to values between $[-\omega_{\max}, \omega_{\max}]$ in degrees ($^\circ$) and translations to $[-d_{\max}, d_{\max}]$ in millimeters (mm). These maximum values are discussed later.

2.1.4 Reward (\mathcal{R})

We defined the following cost function, which includes angular and distance errors:

$$C(t) = \left(1 - \frac{\vec{n}_t \cdot \vec{n}_T}{\|\vec{n}_t\| \|\vec{n}_T\|}\right) + \lambda d(P_t, P_T), \quad (4)$$

where \vec{n}_T and P_T are the normal vector and center point defining the target reformatted plane, respectively. $d(P_t, P_T)$ is the Euclidean distance between P_t and P_T , and λ a scalar that balances the two terms of $C(t)$. We aim to find the set of transitions $T(s_t, a_t, s_{t+1})$ that minimize $C(t)$.

For each transition, we defined the reward as:

$$r_t = -\frac{dC}{dt} = C(t-1) - C(t). \quad (5)$$

Following the negative direction of the gradient of $C(t)$ yields positive rewards until the agent reaches a state close to the target.

2.1.5 Terminal state

The goal of reinforcement learning is to maximize the expected return defined as $R_t = \sum_{k=0}^{\infty} \gamma^k r_{t+k}$, with $\gamma < 1$. In this context, the agent maximizes R_t (i.e., minimizes $C(t)$) with rewards approaching zero as they get closer to the target. This behavior may slow down the agent’s convergence to the target plane location. To address this issue, we defined a “near optimal” state when the angle between \vec{n}_t and \vec{n}_T is less than 3° and the Euclidean distance between P_t and P_T is less than 2 mm. When these conditions are met, the agent receives an additional reward of 3 to accelerate convergence towards the ideal locations of the reformatted planes.

We also defined a terminal state when the current step exceeded t_{\max} . In this case, no extra reward is given to the agent. Upon reaching a terminal state, an initial state is sampled from a new 4D flow MRI dataset, and a new episode begins.

2.2 Reinforcement learning algorithm

Deep Q-Networks (DQN), an off-policy deep reinforcement learning (DRL) algorithm, have been applied to plane reformatting by utilizing past experiences for batch learning [11]. In our framework, these experiences span diverse positions, orientations, and coordinate systems. However, this heterogeneity in the state space can hinder learning by introducing instability and complexity.

In contrast, on-policy algorithms focus on refining a single policy through active exploration, offering improved stability and consistency [15]. To leverage these benefits, we implemented the Asynchronous Advantage Actor-Critic (A3C) algorithm [16]. The agent, modeled as a CNN, estimates a policy $\pi(s, a)$, represented as a normal probability distribution parameterized by the expected value μ_a for each action and its standard deviation σ_a . In addition, the agent estimates a value function $G(s) = \mathbb{E}[R_t | s_t = s]$, indicating the expected return at state $s_t = s$.

The input of the CNN is the current state, structured as a 2-channel array of size $(2, D, H, W)$. The first channel contains the 3D PC-MRA sub-volume, while the second contains V_t . This array goes through four 3D convolutional layers with residual connections (ResNet) [17], creating a 1024×1 latent space representation. This representation is fed into a Long Short Term Memory (LSTM) cell [18], which connects the current state representation with the previous state representation to exploit information between consecutive states.

The LSTM output feeds into three parallel fully connected branches: two actor layers and one critic layer. The first actor layer employs a soft-sign activation to estimate the action mean μ while the second actor layer uses a soft-plus activation to estimate the standard deviation σ . The critic layer computes directly the state-value function $G(s)$. The network was trained with the following gradient:

$$\nabla[\log \pi(a_t | s_t)][F(s_t, a_t) + \eta \nabla H(\pi(s_t))], \quad (6)$$

where $\nabla[\log \pi(a_t | s_t)]$ denotes the gradient direction that increases the probability of action a_t in state s_t . The advantage function $F(s_t, a_t)$ enforces exploitation of the action policy, i.e., estimates if a_t leads to an improvement over the expected return

after k_A steps, and is defined as,

$$F(s_t, a_t) = \sum_{i=0}^{k_A-1} \gamma^i r_{t+i} + \gamma^{k_A} G(s_{t+k_A}) - G(s_t). \quad (7)$$

The entropy $H(\pi(s_t))$ enforces exploration of the action policy, i.e., prevents premature convergence to suboptimal policies, and for a normal distribution is defined as:

$$H(\pi(s_t)) = \sum_{a \in A} \frac{1}{2} (\log_e(2\pi\sigma_a^2) + 1). \quad (8)$$

The coefficient η in equation (6) balances exploration versus exploitation.

A diagram of the reinforcement learning framework is shown in Figure 1.

2.3 Experimental Setup

2.3.1 4D Flow MRI data

We processed a total of 88 anonymized datasets obtained with scanners from different vendors and different institutions including healthy volunteers and patients with congenital heart defects (47 men, 34 ± 12.4 years old) (see Table 1). The patient cohort included individuals with conditions such as coarctation of the aorta (CoA), tetralogy of Fallot (TOF), and bicuspid aortic valve (BAV). These patients represented a range of ages and body sizes but had otherwise normal cardiac anatomy. Authorization from each institution was obtained according to local legislation and ethical compliance. Additional details about each dataset scanning parameters can be found in Appendix A.

Table 1: 4D Flow MRI Datasets

MRI scanner	Number of scans	Description
GE 1.5T	32	Healthy volunteers
GE 1.5T	8	Patients with repaired aortic CoA
GE 1.5T	5	Patients with TOF
Siemens 3T	17	Healthy volunteers
Siemens 3T	8	Patients with BAV
Philips 3T	18	Healthy volunteers

To test our algorithm from all scans, we performed a four-fold cross-validation. For each iteration of cross-validation a blank model was trained with 52 scans ($\sim 59\%$) of each dataset, validated with 14 ($\sim 16\%$), and tested on the remaining 22 (25%). This means that four models were trained to test 25% of data per iteration.

2.3.2 Manually placed planes

For each scan, we used the software Paraview (Kitware, Clifton Park, NY12065, USA) to generate 3D contours of the vessel’s walls using the 3D PC-MRA volume. We also generated velocity vectors within the contours. Two observers (O1 and O2) experienced in 4D flow MRI images used the contours and velocity vectors to place planes in a double oblique orientation [19] at 4 vessels: pulmonary artery (PA), right pulmonary artery (RPA), left pulmonary artery (LPA), and ascending aorta (AAo). They also located a point at the center of the vessels to define P_T as

the target point of the automated plane reformatting. We used the planes placed by the first observer to train the algorithm and the planes placed by the second observer to assess inter-observer variability.

2.3.3 Algorithm parameters

Table 2 lists the empirically chosen parameters for our algorithm. Sub-volumes of size (31,84,84) were selected to cover most structures in the reformatted view. Maximum rotation (5°) and translation (5 mm) values provided smooth transitions to the final reformatted planes, with a 100-step limit to ensure convergence. For network training, λ was set to 0.025 to assign greater error magnitudes to distance compared to angular, encouraging the agent to prioritize adjusting the plane’s location before refining its orientation. The remaining parameters used default A3C values, as changing them did not significantly impact performance.

Table 2: Algorithm Parameters

Name	Value	Description
(D,H,W)	(31,84,84)	Sub-volumes dimensions in pixels
ω_{\max}	5	Maximum rotation in degrees
d_{\max}	5	Maximum translation in mm
t_{\max}	100	Maximum number of steps
λ	0.025	Cost function weight
η	0.01	Loss function entropy weight
k_A	8	Advantage steps

2.3.4 Network training

We trained different CPU workers, each one training a single agent, and updating the parameters of a shared model, allowing the network to learn from policies across multiple volumes, decreasing training time and overfitting. In addition, neural network operations were accelerated with GPU. We used 10 AMD EPYC 7443 CPU cores and 1 Nvidia RTX A6000 GPU for each model (one per plane and cross-validation iteration). Network optimization was performed with Adam optimizer [20] with a constant learning rate of 10^{-5} . We used a Pytorch implementation of A3C, adapted from a public repository [21]. The complete reinforcement learning framework for plane reformatting is available at <https://github.com/JavierBZ/Adaptive-MRI-Plane-Reformatting>

2.4 Algorithm evaluation

2.4.1 Plane reformatting performance

For validation and testing, the algorithm was evaluated for an episode of 100 steps. The model used for testing was the one with the lowest average value of $C(t)$ during validation, i.e., the validation model with the best performance in terms of angular and distance error.

To assess the accuracy of our algorithm, we measured the Euclidean distance between P_{100} and P_T , and the angle between the normal vectors \vec{n}_{100} and \vec{n}_T . The same metrics were evaluated between the annotations of both observers to measure inter-observer variability. We expressed the metrics in terms of mean and standard deviation values (mean \pm standard deviation).

Paired t-tests were performed to analyze differences between algorithm and inter-observer errors.

2.4.2 Flow analysis

To measure flow, we needed a segmentation of the vessel in the reformatted plane. For this we designed a 3-step automatic segmentation procedure: 1) Using the predicted point inside the vessel (P_{100}) we create a disk with a radius of 3 pixels. 2) We moved the disk searching for a location that maximizes the flow through the disk, corresponding to the center of the vessel. 3) We segmented the vessel using active contours in the 3D PC-MRA image [22], as in previous works of hemodynamic quantification [23]. This workflow proved to be effective for most scans. However, a few scans presented difficulties due to the proximity of adjacent vessel walls. To address such cases, we manually corrected the segmentation. Segmentation variability was assessed using the differences in segmented areas as a percentage ratio and Dice scores. Since the segmentations belong to different planes, we first aligned the centers of mass of each segmented area and then evaluated the Dice score [24].

We computed the flow in L/min for each segmented vessel. A regression analysis was used to visualize and quantify the coefficient of determination (R^2) of flow using automated and manually placed planes, as well as to evaluate inter-observer variability. In addition, Bland-Altman plots were used to assess biases and to establish limits of agreement.

Since the obtained flow differences did not have a normal distribution for all planes (verified with a Shapiro-Wilk test), we used a non-parametric paired Wilcoxon test to evaluate statistically significant differences between measurements.

2.4.3 Comparison with baseline method

We implemented the reinforcement learning algorithm for plane reformatting by [11] as a comparative baseline for our framework.

2.4.4 Rotation and translation invariance experiment

To validate the rotation and translation invariance of our algorithm we designed an experiment in which we trained and tested two different models on a single plane of a scan. One model was trained using the baseline DRL method with fixed coordinate system [11], and the other with our proposed framework. After training, we tested both models on the same scan but with different combinations of translations and rotations applied to all axes (translations from -15 mm to 15 mm with 5 mm intervals and rotations from -15° to 15° with 5° intervals). Finally, we compared the mean and standard deviations of angular and distance error.

2.4.5 Analysis software

Regression analysis and Bland-Altman plots were performed using GraphPad Prism v.9 (GraphPad Software, La Jolla, CA). Statistical analyses were performed in R (R Development Core Team; <https://www.R-project.org>) with a significance level of $p < 0.05$.

3 Results

3.1 Plane Reformatting Performance

For all datasets, the estimated planes defined by our algorithm and the manually placed planes by the first observer (O1) yielded an angular error of $6.32 \pm 4.15^\circ$ and distance error of 3.40 ± 2.75 mm. Comparing with the second observer (O2), the angular error was $7.28 \pm 4.70^\circ$ and distance error was 4.03 ± 3.10 mm. For inter-observer variability, we obtained an angular error of $4.42 \pm 4.48^\circ$ and a distance error of 3.11 ± 2.98 mm (Table 3).

Paired t-tests between errors of our algorithm vs. O1 and inter-observer errors showed a significant difference only for angular errors ($p < 0.05$), whereas no significant difference was observed for distance errors ($p = 0.57$). Paired t-test between errors of our algorithm vs. O2 and inter-observer errors showed a significant difference for both angular and distance errors ($p < 0.05$). For the AAO and LPA planes, errors of our algorithm vs. O1 and inter-observer errors showed no significant difference in both angular ($p = 0.09$ for AAO, $p = 0.21$ for LPA) and distance ($p = 0.68$ for AAO, $p = 0.07$ for LPA) errors. However, for RPA and PA planes, there was a significant difference for angular and distance errors ($p < 0.05$). Errors of our algorithm vs. O2 errors and inter-observer errors showed significant differences except for the distance error in the AAO plane ($p = 0.29$).

When analyzing only healthy volunteers, we obtained errors of $6.00 \pm 4.17^\circ$ and 3.11 ± 2.36 mm between planes placed by our algorithm and those placed by O1. The inter-observer errors were $4.51 \pm 4.25^\circ$ and 3.08 ± 2.72 mm.

For patients (bicuspid aortic valve, tetralogy of Fallot, and aortic coarctation) we obtained errors of $7.31 \pm 3.98^\circ$ and 4.36 ± 3.58 mm between planes placed by our algorithm and those placed by O1. The inter-observer errors were $4.14 \pm 5.14^\circ$ and 3.21 ± 3.70 mm.

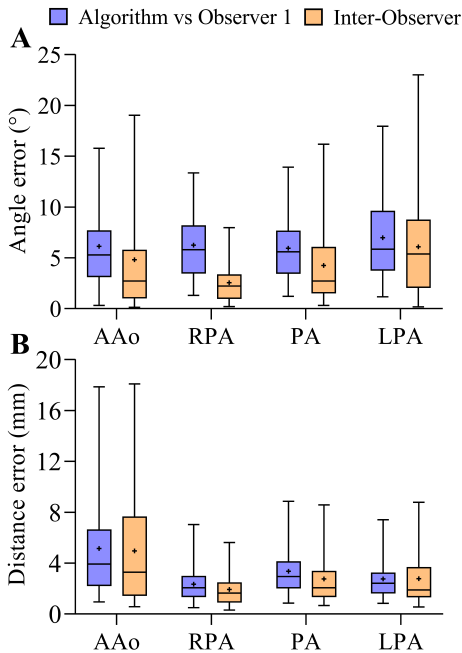


Figure 2: Distribution of plane reformatting metrics. Whiskers range from the 2.5th to the 97.5th percentile. The line represents the median, and the dot represents the mean. (A) Angular error ($^\circ$). (B) Distance error (mm).

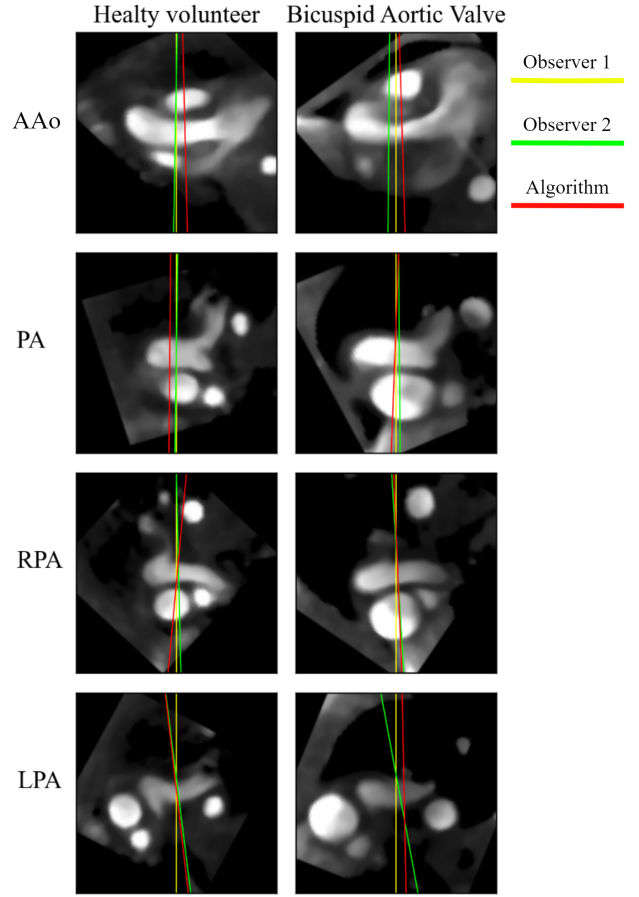


Figure 3: Examples of plane reformatting. O1, O2, and algorithm planes are shown in yellow, green, and red, respectively. The first column shows planes for a healthy volunteer and the second column for a BAV patient.

From boxplots (Figure 2) we can see that although the mean and median of AAO and LPA planes are higher for algorithm vs. O1, box sizes and whiskers range are narrower compared to the inter-observer boxplots. For RPA and PA planes the box sizes and whiskers range appear to be similar to those seen in the inter-observer boxplots.

Reformatting the plane PA was the one with the lowest angular error ($5.93 \pm 3.21^\circ$) and the worst was the LPA plane ($6.97 \pm 4.33^\circ$). Reformatting the plane RPA was the one with the lowest distance error (2.34 ± 1.44 mm) and the worst was the AAO plane (5.15 ± 4.03 mm).

3.2 Flow Analysis

Similar coefficients of determination (R^2) were obtained for flow measurements of all planes when comparing our algorithm with O1 and the R^2 between observers (0.931 vs. 0.939). This indicates good agreement between measurements (Table 4).

The analysis indicated no significant difference between all flow measurements obtained with our algorithm and those obtained by O1 ($p = 0.21$). However, analyzing only the flow measurements for the LPA plane, there was a significant difference ($p < 0.05$). On the other hand, a significant difference was observed in all flow measurements between O1 and O2 ($p < 0.05$).

Regarding segmentation variability, we found an average difference ratio of 7.8%, and a Dice score of 0.916 between areas obtained with our algorithm and O1. For inter-observer variabil-

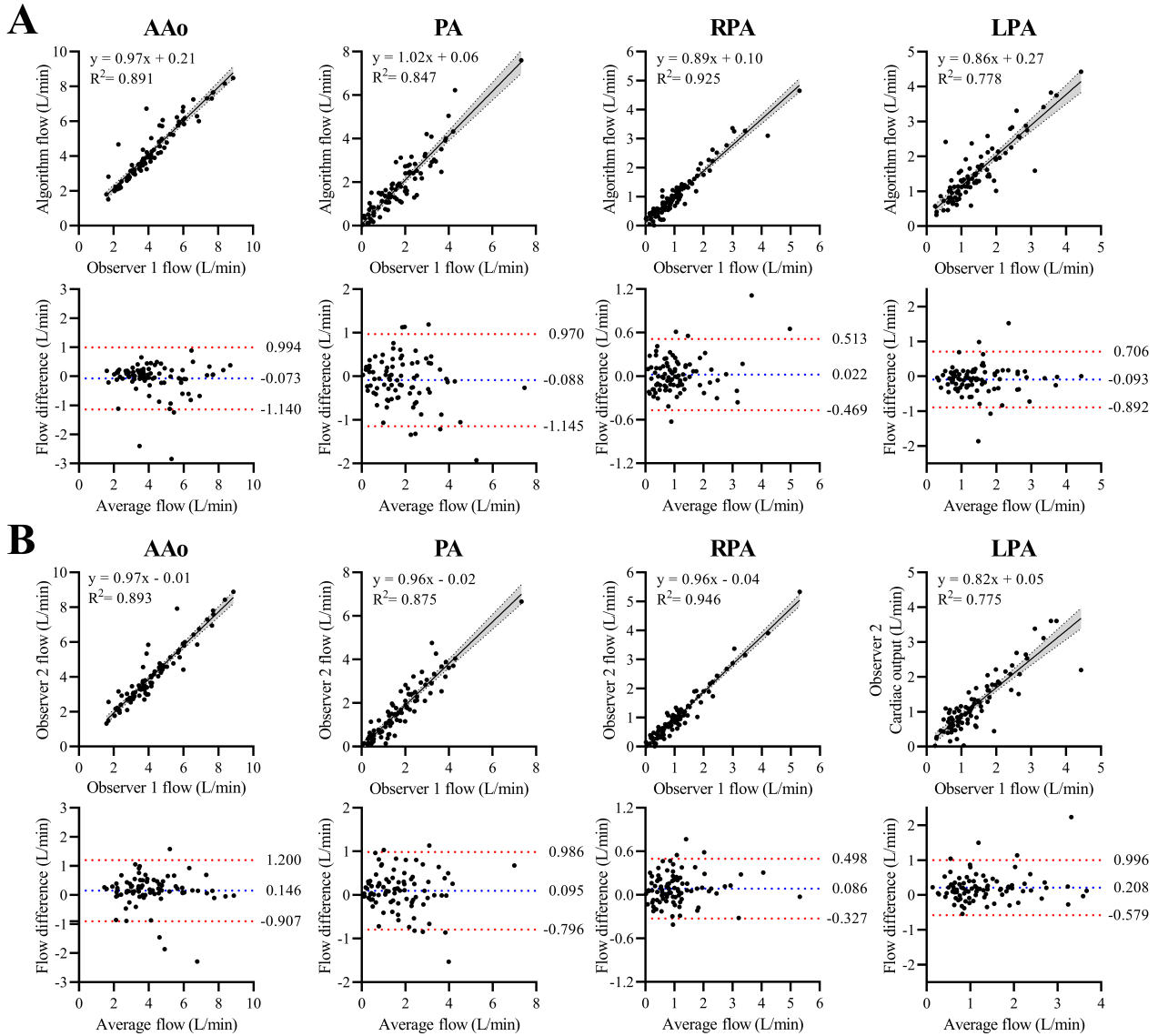


Figure 4: Regression analysis with shaded area representing 95% confidence interval, and Bland-Altman plots. Differences of Bland Altman plots **A**, O1 flows v/s algorithm flows (Bland-Altman differences O1 flow L/min - algorithm flow L/min). **B**, O1 flows v/s O2 flows (Bland-Altman differences O1 flow L/min - O2 flow L/min).

Table 3: Metrics for reformatted planes: Our algorithm vs first observer and inter-observer errors. † denotes significant difference ($p < 0.05$) between algorithm errors (first and second row) and inter-observer errors.

Group	Metric	AAo	PA	RPA	LPA	All
Our algorithm vs Observer 1	Angular error (°)	6.13 ± 5.50	5.93 ± 3.21†	6.25 ± 3.11†	6.97 ± 4.33	6.32 ± 4.15†
	Distance error (mm)	5.15 ± 4.03	3.35 ± 1.90†	2.34 ± 1.44†	2.76 ± 1.98	3.40 ± 2.75
Our algorithm vs Observer 2	Angular error (°)	6.95 ± 5.83†	7.06 ± 3.98†	6.22 ± 3.10†	8.91 ± 5.06†	7.28 ± 4.70†
	Distance error (mm)	5.68 ± 4.55	3.88 ± 2.14†	2.50 ± 1.49†	4.06 ± 2.48†	4.03 ± 3.10†
Inter-observer	Angular error (°)	4.64 ± 5.07	4.25 ± 4.03	2.56 ± 2.25	6.08 ± 4.96	4.42 ± 4.48
	Distance error (mm)	4.96 ± 4.51	2.76 ± 1.99	1.93 ± 1.43	2.78 ± 2.09	3.11 ± 2.98

ity we found an average area difference ratio of 6.7% and a Dice score of 0.919. Bland-Altman analysis showed that the average bias of the differences between flows measured by O1 and those calculated by our algorithm had a smaller range compared to the bias between the observers (-0.058 L/min and 0.134 L/min, re-

spectively). However, average limits of agreement were wider for differences between O1 and the algorithm than between observers (1.707 L/min and 1.573 L/min, respectively).

Table 4: Flow analysis. The first three rows show average and standard deviation of flows measured by our algorithm and observers. The fifth and sixth rows show the coefficient of determination (R^2) of linear regression between flow measurements. The sixth and seventh rows contain p -values of differences between flow measurements. The last column summarizes all planes.

Metric	AAo	PA	RPA	LPA	All
Flow O1 (L/min)	4.15 ± 1.59	1.75 ± 1.23	1.13 ± 0.90	1.41 ± 0.84	2.12 ± 1.69
Flow O2 (L/min)	4.00 ± 1.63	1.66 ± 1.27	1.05 ± 0.89	1.21 ± 0.78	1.98 ± 1.69
Flow algorithm (L/min)	4.22 ± 1.63	1.84 ± 1.37	1.11 ± 0.84	1.51 ± 0.83	2.17 ± 1.72
R^2 O1 vs algorithm	0.891	0.847	0.925	0.778	0.931
R^2 O1 vs O2	0.893	0.875	0.946	0.775	0.939
p -value O1 vs algorithm	0.158	0.154	0.766	0.013	0.212
p -value O1 vs O2	$6.3 \cdot 10^{-7}$	$9.0 \cdot 10^{-3}$	$2.2 \cdot 10^{-4}$	$1.8 \cdot 10^{-6}$	$8.3 \cdot 10^{-16}$

3.3 Comparison with Baseline Method

Compared with the baseline method DQN for plane reformatting [11], our method had significantly better performance in angular ($23.2 \pm 7.3^\circ$ vs. $6.3 \pm 4.2^\circ$) and distance error (8.0 ± 7.1 mm vs. 3.4 ± 2.8 mm). We did not measure flow with the baseline method because most reformatted planes did not locate the correct vessel to perform the segmentation.

3.4 Rotation and Translation Invariance Experiment

For different combinations of rotations and translations, the DQN algorithm obtained an average angular error of $46.41 \pm 23.11^\circ$ and 14.58 ± 12 mm for distance error. This average error differs from the error with no rotations and translations (3.95° and 1.19 mm). Our algorithm performed better obtaining an average angular error of $2.49 \pm 1.06^\circ$ and 1.21 ± 0.43 mm for distance error, with 1.86° and 0.83 mm for no rotations and translations.

3.5 Training and Evaluation Times

Training the algorithm for one plane took 24 hours on average using 10 CPU cores and 1 GPU. Depending on available resources, more CPU cores or GPUs could accelerate the training process without compromising performance. Pre-processing the volumes of one scan took 3–5 seconds on average, and evaluation 3–4 seconds per plane.

4 Discussion

4.1 Plane Reformatting

Our framework provides good performance for plane reformatting, offering flexibility to process volumes with varied fields of view and orientations without compromising accuracy. As exhibited in our rotation and translation invariance experiment (Section 2.4.4), our method maintains consistent performance across different positions and orientations for a single volume, whereas DQN [11] exhibited unstable results due to inconsistencies in expected transitions.

Landmark-based methods face similar limitations. The best-performing cardiac MRI method uses a CNN to locate landmarks within the mitral valve slice [8], but this restricts its application to short-axis oriented volumes. Similarly, DRL-based landmark lo-

Table 5: Comparison with previous methods.

Method	Data type	Distance error (mm)	Angular error ($^\circ$)	Flow aorta (R^2)
Proposed framework	4D Flow MRI	3.4 ± 2.8	6.3 ± 4.2	0.89
3D CNN [10]	4D Flow MRI	$9.0 \pm 7.3^\dagger$	$12.3 \pm 7.2^\dagger$	0.74
Atlas registration [9]	4D Flow MRI	*	*	0.93
DQN [11]	Cardiac Cine MRI	$5.1 \pm 3.0^\dagger$	$8.7 \pm 7.4^\dagger$	-
DL landmarks [8]	Cardiac Cine MRI	$7.5 \pm 8.2^\dagger$	6.4 ± 5.9	-

* Values not reported.

† Denotes significance difference ($p < 0.05$) compared to the proposed framework.

calization methods perform 3D trajectories within a volume with actions that are also restricted to a fixed orientation [25, 26].

While rigid or affine registration methods can standardize orientation and position [27], their success depends on volume similarity. Differences in resolution, field of view, orientation, or anatomy, especially those caused by heart malformations, can limit their generalizability.

To compare our method against previously reported methods, we compared average performance across all analyzed planes within each study (Table 5). Differences in distance error and angular error were assessed using the t-test, using the mean, deviation, and number of samples of each publication. For methods using 4D flow MRI, we compared R^2 values of flow measurements in the ascending aorta.

We found statistically improved metrics compared to previous methods ($p < 0.05$), except for DL landmark localization [8] regarding angular error ($p = 0.84$), where we achieved a similar average angular error, but with a lower deviation.

There is still a gap in improvement given our inter-observer variability in plane reformatting, especially for angular error, where we found a significant difference between overall inter-observer errors and our algorithm errors. These differences are mainly found in RPA and PA. Collaborative agents [13] could potentially reduce variability and improve performance. It’s important to acknowledge varying inter-observer variabilities reported across studies; for example, Corrado et al. [10] reported signifi-

cantly higher inter-observer variability (8.3 ± 5.8 mm for distance error, $13.9 \pm 7.8^\circ$ for angular error) than ours. Efforts towards clinically validated benchmarks for plane reformatting will allow a fair comparison.

A key advantage of our approach is its adaptability beyond 4D flow MRI. By learning from volumetric navigation rather than fixed landmarks, it can be applied to other modalities such as MRI/CT angiography or 3D ultrasound, enabling broad clinical and research applications in plane localization and reformatting.

4.2 Flow Measurements

Our method achieved better flow agreement in the aorta than the deep learning-based 4D flow MRI approach [10], though slightly worse than atlas-based registration [9]. However, atlas-based methods depend heavily on image similarity. For example, Bustamante et al. [9] excluded outlier cases with poor registration, introducing selection bias. While the authors propose using multiple atlases to address this issue, this approach becomes impractical due to the diversity of potential heart malformations.

In contrast, our method can work with both healthy and heart malformations. Although errors were slightly higher for patients (1.3° and 1.3 mm), this may reflect the lower proportion of patient data (21 patients, corresponding to 24% of the data). Increasing patient data should help reduce this difference.

We observed no significant difference between all measurements using planes obtained with our algorithm and O1 planes ($p = 0.21$). However, we found a significant difference analyzing only flow measurements in LPA ($p < 0.05$). Surprisingly, despite observers having less average angular and distance errors than our algorithm, we found significant differences in flow measurements between observers ($p < 0.05$). While inter-observer angular and distance errors were lower on average, their deviations and bias were higher, as illustrated in the boxplots and Bland-Altman plots. This suggests that a subset of planes with larger discrepancies may influence the statistical outcomes.

Flow quantification in 4D flow MRI remains susceptible to limitations such as noise, artifacts, and spatial resolution [28]. Differences in segmentation also impact flow results. A recent study demonstrated that $\pm 17\%$ of changes in the area of segmentation caused significant changes in flow, nearly 20% for both forward and backward volumes [29]. Although our study had lower segmentation differences ratios (7.8% O1 vs. algorithm, and 6.7% between observers) and high Dice scores (0.916 O1 vs. algorithm, and 0.918 between observers), a combination of these factors, along with angular and distance error, could potentially result in significant flow disparities.

Unlike manual plane reformatting, which relies solely on visual expertise, our algorithm analyzes both vessel structures and velocity values. The algorithm likely seeks a plane with representative structures and velocity profiles for each vessel, which may be in a different position than the manual plane. This could explain why, despite the algorithm having larger angular and distance error than between observers, the reformatted planes still yielded similar velocities.

4.3 Limitations

Our framework relies on supervised training, meaning the accuracy of plane reformatting depends heavily on two key factors: the size and diversity of the training data and the quality of the

manual labels used for supervision. To enhance performance, future work could incorporate additional training objectives, such as maximizing through-plane flow, to reduce biases introduced by limited datasets or imperfect labels. Further evaluation in patients with discordant or complex cardiac anatomy is also needed to confirm our method’s generalizability.

A limitation of this study is the relatively small dataset, comprising 88 scans with only 25 percent from patients. Expanding medical imaging datasets is inherently challenging due to strict privacy regulations and the labor-intensive nature of manual annotation. As dataset sizes increase, manual labeling becomes increasingly impractical, posing a persistent challenge in medical image analysis.

In addition, pre-processing is required when evaluating new datasets, including contrast enhancement and interpolation to isotropic resolution. While these steps aim to reduce variability in contrast and resolution across datasets, they may discard valuable information that could improve the accuracy of plane reformatting.

5 Conclusion

We have developed a robust plane reformatting framework that effectively overcomes limitations caused by volume variability due to different positions and orientations, outperforming previous reformatting methods. The method was validated in 4D flow MRI, revealing no significant disparities in automated flow quantification compared to manual quantification.

A Appendix A

Due to privacy concerns, we are unable to share the images used to train and test the algorithm. The 4D Flow MRI datasets in this study were acquired as follows:

32 scans from healthy volunteers were obtained in a clinical GE 1.5T Signa scanner (GE Healthcare, Waukesha, WI, USA) using the Vastly undersampled Isotropic Projection Reconstruction (VIPR) technique [30]. Imaging parameters included a field of view (FOV) $400 \text{ mm} \times 400 \text{ mm} \times 400 \text{ mm}$, voxel size of $2.5 \text{ mm} \times 2.5 \text{ mm} \times 2.5 \text{ mm}$, flip angle 8° , repetition time 4.2–6.4 ms, echo time 1.9–3.7 ms, and velocity encoding 200 cm/s. This dataset was reconstructed with a temporal resolution that ranged between 21–32 ms.

8 scans from repaired aortic coarctation and 5 from tetralogy of Fallot were obtained using GE 1.5T Optima scanner (GE Healthcare, Waukesha, WI, USA). 4D-flow imaging parameters were as follows: spatial resolution (row \times column \times slice) = $2.34 \times 2.34 \times 2.5 \text{ mm}^3$, temporal resolution = 37.62 ± 4.43 ms, flip angle = 5° ; field of view (FOV) = $236 \times 226 \times 134 \text{ mm}$, velocity sensitivity (Venc) = 250 cm/s, echo time = 2.66 ms, pulse repetition time = 4.78–4.80 ms.

17 scans from healthy volunteers and 8 from bicuspid aortic valve patients were obtained in a 3T Prisma scanner (Siemens, Erlangen, Germany). ECG-gated 4D-flow MRI (WIP 785A) was acquired during free breathing using navigator gating of diaphragmatic motion [31]. 4D-flow imaging parameters were as follows: spatial resolution (row \times column \times slice) = $2.0\text{--}2.5 \times 2.0\text{--}2.5 \times 2.4\text{--}3.5 \text{ mm}^3$, temporal resolution = 36.24–40.56 ms, flip angle = 15° ; field of view (FOV) = $240\text{--}350 \times 320\text{--}400 \text{ mm}^2$, bandwidth = 455–495 Hz/Pixel, velocity sensitivity (Venc)

= 150–550 cm/s, echo time = 2.01–2.35 ms, pulse repetition time = 4.53–5.07 ms.

18 scans from healthy volunteers were obtained in a 3T Philips MRI scanner (Philips Achieva, Best, The Netherlands). 4D-flow imaging parameters were as follows: spatial resolution (row \times column \times slice) = $2.34 \times 2.34 \times 2.5 \text{ mm}^3$, temporal resolution = $37.62 \pm 4.43 \text{ ms}$, flip angle = 5° ; field of view (FOV) = $236 \times 226 \times 134 \text{ mm}$, velocity sensitivity (Venc) = 250 cm/s, echo time = 2.66 ms, pulse repetition time = 4.78–4.80 ms.

Acknowledgment

J.B. was funded by the National Agency for Research and Development (ANID) / Scholarship Program / DOCTORADO BECAS CHILE/2022 – 21220454, and by ANID - Millennium Science Initiative Program - ICN2021_004. J.S. Thanks to ANID-FONDECYT de iniciación en investigación 11200481 and the Department of Medical Imaging and Radiation Sciences at Monash University. C.T. thanks Fondecyt 1231535 and ANID - Millennium Science Initiative Program - ICN2021_004. P.I. thanks to Fondecyt 1210747.

References

- [1] Julio Sotelo, Israel Valverde, Duarte Martins, Damien Bonnet, Nathalie Boddaert, Kuberan Pushparajan, Sergio Uribe, and Francesca Raimondi. Impact of aortic arch curvature in flow haemodynamics in patients with transposition of the great arteries after arterial switch operation. *European Heart Journal - Cardiovascular Imaging*, 23(3):402–411, February 2022.
- [2] Francesca Raimondi, Duarte Martins, Raluca Coenen, Elena Panaioli, Diala Khraiche, Nathalie Boddaert, Damien Bonnet, Melany Atkins, Howaida El-Said, Laith Alshawabkeh, and Albert Hsiao. Prevalence of Venovenous Shunting and High-Output State Quantified with 4D Flow MRI in Patients with Fontan Circulation. *Radiology: Cardiothoracic Imaging*, 3(6):e210161, December 2021.
- [3] Julio Sotelo, Pamela Franco, Andrea Guala, Lydia Dux-Santoy, Aroa Ruiz-Muñoz, Arturo Evangelista, Hernan Mella, Joaquín Mura, Daniel E. Hurtado, José F. Rodríguez-Palomares, and Sergio Uribe. Fully Three-Dimensional Hemodynamic Characterization of Altered Blood Flow in Bicuspid Aortic Valve Patients With Respect to Aortic Dilatation: A Finite Element Approach. *Frontiers in Cardiovascular Medicine*, 9:885338, May 2022.
- [4] Sergio Uribe, Philipp Beerbaum, Thomas Sangild Sørensen, Allan Rasmusson, Reza Razavi, and Tobias Schaeffter. Four-dimensional (4D) flow of the whole heart and great vessels using real-time respiratory self-gating: Real-Time Self-Gating 4D Flow Imaging. *Magnetic Resonance in Medicine*, 62(4):984–992, October 2009.
- [5] Malenka M. Bissell, Francesca Raimondi, Lamia Ait Ali, Bradley D. Allen, Alex J. Barker, Ann Bolger, Nicholas Burris, Carl-Johan Carhäll, Jeremy D. Collins, Tino Ebbers, Christopher J. Francois, Alex Frydrychowicz, Pankaj Garg, Julia Geiger, Hojin Ha, Anja Hennemuth, Michael D. Hope, Albert Hsiao, Kevin Johnson, Sebastian Kozerke, Liliana E. Ma, Michael Markl, Duarte Martins, Marci Messina, Thekla H. Oechtering, Pim Van Ooij, Cynthia Rigsby, Jose Rodriguez-Palomares, Arno A. W. Roest, Alejandro Roldán-Alzate, Susanne Schnell, Julio Sotelo, Matthias Stuber, Ali B. Syed, Johannes Töger, Rob Van Der Geest, Jos Westenberg, Liang Zhong, Yumin Zhong, Oliver Wieben, and Petter Dyverfeldt. 4D Flow cardiovascular magnetic resonance consensus statement: 2023 update. *Journal of Cardiovascular Magnetic Resonance*, 25(1):40, July 2023.
- [6] Liang Zhong, Eric M. Schrauben, Julio Garcia, Sergio Uribe, Stuart M. Grieve, Mohammed S.M. Elbaz, Alex J. Barker, Julia Geiger, Sarah Nordmeyer, Alison Marsden, Marcus Carlsson, Ru-San Tan, Pankaj Garg, Jos J.M. Westenberg, Michael Markl, and Tino Ebbers. Intracardiac 4D Flow MRI in Congenital Heart Disease: Recommendations on Behalf of the ISMRM Flow & Motion Study Group. *Journal of Magnetic Resonance Imaging*, 50(3):677–681, September 2019.
- [7] Marc-Antoine Isorni, Louis Moisson, Nidal Ben Moussa, Sébastien Monnot, Francesca Raimondi, Régine Roussin, Angèle Boet, Isabelle Van Aerschot, Emmanuelle Fournier, Sarah Cohen, Meriem Kara, and Sébastien Hascoet. 4D flow cardiac magnetic resonance in children and adults with congenital heart disease: Clinical experience in a high volume center. *International Journal of Cardiology*, 320:168–177, December 2020.
- [8] Kevin Blansit, Tara Retson, Evan Masutani, Naeim Bahrami, and Albert Hsiao. Deep Learning–based Prescription of Cardiac MRI Planes. *Radiology: Artificial Intelligence*, 1(6):e180069, November 2019.
- [9] Mariana Bustamante, Sven Petersson, Jonatan Eriksson, Urban Alehagen, Petter Dyverfeldt, Carl-Johan Carlhäll, and Tino Ebbers. Atlas-based analysis of 4D flow CMR: Automated vessel segmentation and flow quantification. *Journal of Cardiovascular Magnetic Resonance*, 17(1):87, January 2015.
- [10] Philip A. Corrado, Daniel P. Seiter, and Oliver Wieben. Automatic measurement plane placement for 4D Flow MRI of the great vessels using deep learning. *International Journal of Computer Assisted Radiology and Surgery*, 17(1):199–210, January 2022.
- [11] Amir Alansary, Loic Le Folgoc, Ghislain Vaillant, Ozan Oktay, Yuanwei Li, Wenjia Bai, Jonathan Passerat-Palmbach, Ricardo Guerrero, Konstantinos Kamnitsas, Benjamin Hou, Steven McDonagh, Ben Glocker, Bernhard Kainz, and Daniel Rueckert. Automatic View Planning with Multi-scale Deep Reinforcement Learning Agents, June 2018. arXiv:1806.03228 [cs].
- [12] Haoran Dou, Xin Yang, Jikuan Qian, Wufeng Xue, Hao Qin, Xu Wang, Lequan Yu, Shujun Wang, Yi Xiong, Pheng-Ann Heng, and Dong Ni. Agent with Warm Start and Active Termination for Plane Localization in 3D Ultrasound, October 2019. arXiv:1910.04331 [cs, eess].

- [13] Yuhao Huang, Xin Yang, Rui Li, Jikuan Qian, Xiaoqiong Huang, Wenlong Shi, Haoran Dou, Chaoyu Chen, Yuanji Zhang, Huanjia Luo, Alejandro Frangi, Yi Xiong, and Dong Ni. Searching Collaborative Agents for Multi-plane Localization in 3D Ultrasound, July 2020. arXiv:2007.15273 [cs, eess].
- [14] Stephen M Pizer, E Philip Amburn, John D Austin, Robert Cromartie, Ari Geselowitz, Trey Greer, Bart ter Haar Romeny, John B Zimmerman, and Karel Zuiderveld. Adaptive histogram equalization and its variations. *Computer vision, graphics, and image processing*, 39(3):355–368, 1987. Publisher: Elsevier.
- [15] Ivo Grondman, Lucian Busoniu, Gabriel A. D. Lopes, and Robert Babuska. A Survey of Actor-Critic Reinforcement Learning: Standard and Natural Policy Gradients. *IEEE Transactions on Systems, Man, and Cybernetics, Part C (Applications and Reviews)*, 42(6):1291–1307, November 2012.
- [16] Volodymyr Mnih, Adrià Puigdomènech Badia, Mehdi Mirza, Alex Graves, Timothy P. Lillicrap, Tim Harley, David Silver, and Koray Kavukcuoglu. Asynchronous Methods for Deep Reinforcement Learning, June 2016. arXiv:1602.01783 [cs].
- [17] Kaiming He, Xiangyu Zhang, Shaoqing Ren, and Jian Sun. Deep Residual Learning for Image Recognition. In *2016 IEEE Conference on Computer Vision and Pattern Recognition (CVPR)*, pages 770–778, Las Vegas, NV, USA, June 2016. IEEE.
- [18] Sepp Hochreiter and Jürgen Schmidhuber. Long Short-Term Memory. *Neural Computation*, 9(8):1735–1780, November 1997.
- [19] Matt Morgan. Double oblique multiplanar reconstruction, November 2014.
- [20] Diederik P. Kingma and Jimmy Ba. Adam: A Method for Stochastic Optimization, January 2017. arXiv:1412.6980 [cs].
- [21] Ilya Kostrikov. PyTorch Implementations of Asynchronous Advantage Actor Critic, 2018. Publication Title: GitHub repository.
- [22] T.F. Chan and L.A. Vese. Active contours without edges. *IEEE Transactions on Image Processing*, 10(2):266–277, February 2001.
- [23] Cristian Montalba, Jesus Urbina, Julio Sotelo, Marcelo E. Andía, Cristian Tejos, Pablo Irarrazaval, Daniel E. Hurtado, Israel Valverde, and Sergio Uribe. Variability of 4D flow parameters when subjected to changes in MRI acquisition parameters using a realistic thoracic aortic phantom. *Magnetic Resonance in Medicine*, 79(4):1882–1892, April 2018.
- [24] Lee R. Dice. Measures of the Amount of Ecologic Association Between Species. *Ecology*, 26(3):297–302, July 1945.
- [25] Walid Abdullah Al and Il Dong Yun. Partial Policy-Based Reinforcement Learning for Anatomical Landmark Localization in 3D Medical Images. *IEEE Transactions on Medical Imaging*, 39(4):1245–1255, April 2020.
- [26] Amir Alansary, Ozan Oktay, Yuanwei Li, Loic Le Folgoc, Benjamin Hou, Ghislain Vaillant, Konstantinos Kamnitsas, Athanasios Vlontzos, Ben Glocker, Bernhard Kainz, and Daniel Rueckert. Evaluating reinforcement learning agents for anatomical landmark detection. *Medical Image Analysis*, 53:156–164, April 2019.
- [27] Francisco P.M. Oliveira and João Manuel R.S. Tavares. Medical image registration: a review. *Computer Methods in Biomechanics and Biomedical Engineering*, 17(2):73–93, January 2014.
- [28] Petter Dyverfeldt, Malenka Bissell, Alex J. Barker, Ann F. Bolger, Carl-Johan Carlhäll, Tino Ebbers, Christopher J. Francios, Alex Frydrychowicz, Julia Geiger, Daniel Giese, Michael D. Hope, Philip J. Kilner, Sebastian Kozerke, Saul Myerson, Stefan Neubauer, Oliver Wieben, and Michael Markl. 4D flow cardiovascular magnetic resonance consensus statement. *Journal of Cardiovascular Magnetic Resonance*, 17(1):72, December 2015.
- [29] M E Casciaro, A F Pascaner, F N Guilenea, J Alcibar, U Gencer, G Soulat, E Mousseaux, and D Craiem. 4D flow MRI: impact of region of interest size, angulation and spatial resolution on aortic flow assessment. *Physiological Measurement*, 42(3):035004, March 2021.
- [30] Tianliang Gu, Frank R Korosec, Walter F Block, Sean B Fain, Quill Turk, Darren Lum, Yong Zhou, Thomas M Grist, Victor Haughton, and Charles A Mistretta. PC VIPR: A High-Speed 3D Phase-Contrast Method for Flow Quantification and High- Resolution Angiography. 2005.
- [31] Julio Garcia, Kailey Beckie, Ali F Hassanabad, Alireza Soudji, and James A White. Aortic and mitral flow quantification using dynamic valve tracking and machine learning: Prospective study assessing static and dynamic plane repeatability, variability and agreement. *JRSM Cardiovascular Disease*, 10:204800402199990, January 2021.